Article

Prion Protein—Antibody Complexes Characterized by Chromatography-Coupled Small-Angle X-Ray Scattering

Lester Carter,[1] Seung Joong Kim,[2] Dina Schneidman-Duhovny,[2] Jan Stöhr,[3,4] Guillaume Poncet-Montange,[3] Thomas M. Weiss,[1] Hiro Tsuruta,[1] Stanley B. Prusiner,[3,4,*] and Andrej Sali[2,*]

[1]Stanford Synchrotron Radiation Lightsource, SLAC National Accelerator Laboratory, Menlo Park, California; [2]Department of Bioengineering and Therapeutic Sciences and Department of Pharmaceutical Chemistry and California Institute for Quantitative Biosciences (QB3), [3]Institute for Neurodegenerative Diseases, and [4]Department of Neurology, University of California San Francisco, San Francisco, California

ABSTRACT Aberrant self-assembly, induced by structural misfolding of the prion proteins, leads to a number of neurodegenerative disorders. In particular, misfolding of the mostly α-helical cellular prion protein (PrP^C) into a β-sheet-rich disease-causing isoform (PrP^{Sc}) is the key molecular event in the formation of PrP^{Sc} aggregates. The molecular mechanisms underlying the PrP^C-to-PrP^{Sc} conversion and subsequent aggregation remain to be elucidated. However, in persistently prion-infected cell-culture models, it was shown that treatment with monoclonal antibodies against defined regions of the prion protein (PrP) led to the clearing of PrP^{Sc} in cultured cells. To gain more insight into this process, we characterized PrP-antibody complexes in solution using a fast protein liquid chromatography coupled with small-angle x-ray scattering (FPLC-SAXS) procedure. High-quality SAXS data were collected for full-length recombinant mouse PrP [denoted recPrP(23–230)] and N-terminally truncated recPrP(89–230), as well as their complexes with each of two Fab fragments (HuM-P and HuM-R1), which recognize N- and C-terminal epitopes of PrP, respectively. In-line measurements by fast protein liquid chromatography coupled with SAXS minimized data artifacts caused by a non-monodispersed sample, allowing structural analysis of PrP alone and in complex with Fab antibodies. The resulting structural models suggest two mechanisms for how these Fabs may prevent the conversion of PrP^C into PrP^{Sc}.

INTRODUCTION

Prion diseases are caused by proteins in an alternatively folded, self-replicating conformation of a host-encoded protein (1). As soon as these proteins misfold, they start to recruit more proteins into the same conformation through conformational templating (2). Misfolding of the prion precursor protein occurs spontaneously but may be hastened by prion protein (PrP) mutations or, rarely, via exposure to exogenous prions through infection. Irrespective of the etiology, misfolding results in multiplication of the disease-causing isoform (PrP^{Sc}), which spreads throughout the brain and other organs (3,4). Recent findings have demonstrated that many neurodegenerative diseases, such as Creutzfeldt-Jakob, Alzheimer's, and Parkinson's diseases, as well as the frontotemporal dementias, are all caused by proteins that become prions, accumulate, and cause disease (5). To date, no treatment is available to revert, stop, or even delay the clinical course of any of these disorders (6).

Mammalian PrP was the first protein to be discovered that can convert into a prion conformation (7). Its alternatively folded isoform, designated PrP^{Sc}, causes Creutzfeldt-Jakob disease in humans, bovine spongiform encephalopathy in cattle, and scrapie in sheep (5). PrP^{Sc} is formed from its cellular PrP precursor (PrP^C) by a profound conformational change (8,9). PrP^{Sc} is insoluble and partially resistant to proteases, whereas PrP^C is soluble and sensitive to protease digestion (9,10). The detailed mechanisms underlying the conversion of PrP^C into PrP^{Sc} and subsequent aggregation into higher-order aggregates are still unknown.

PrP^C is membrane-bound and seems likely to be involved in cellular adhesion and signaling (11). PrP^C consists of two domains, a disordered N-terminal domain (residues 23–124) and a globular C-terminal domain composed of three α-helices and two short antiparallel β-strands (residues 125–230). Structural studies using solution NMR spectroscopy and x-ray crystallography revealed the structure of the C-terminal domain (12–17), but neither the structure of the flexible N-terminal domain of PrP^C nor the structure of PrP^{Sc} is known (18).

Although no treatments exist for PrP prion diseases, studies have shown that antibodies directed against certain regions (including residues 95–110 and 221–230) are effective in clearing PrP^{Sc} from chronically infected cultured cells, whereas antibodies against more N-terminal residues were largely ineffective (19,20). In one study, treatment

Submitted February 12, 2015, and accepted for publication June 30, 2015.

*Correspondence: sali@salilab.org or stanley@ind.ucsf.edu

Hiro Tsuruta died on August 25, 2011.

Lester Carter, Seung Joong Kim, Dina Schneidman-Duhovny, and Jan Stöhr contributed equally to this work.

Guillaume Poncet-Montange's present address is Department of Genomic Medicine, University of Texas, MD Anderson Cancer Center, 1515 Holcombe Blvd. Unit 1000, Houston, TX 77030.

Editor: Lois Pollack.

0006-3495/15/08/0793/13

http://dx.doi.org/10.1016/j.bpj.2015.06.065

of mice with these antibodies triggered neuronal apoptosis. This result was believed to be due to antibody-induced cross-linking (21), but could not be recapitulated in follow-up studies (20). Therefore, passive immunization was suggested to be a potential treatment for prion diseases (20). Even though antibodies were able to clear cell culture systems of prion infection successfully, the underlying mechanism remains to be determined.

To obtain more information about the structure of PrP in complex with these antibodies, we structurally characterized these complexes using small-angle x-ray scattering (SAXS). In particular, we focused on potential antibody-induced structural transitions that might prevent or modify the PrP^{C}-to-PrP^{Sc} conversion. SAXS provides comprehensive structural information about macromolecules in solution, including molecular shape and structural variability (22–24). SAXS exploits the elastic scattering of protein atoms in solution to produce a one-dimensional intensity profile that is a function of spatial frequency. The profile can be converted into an approximate distribution of pairwise electron distances in the macromolecule (i.e., the pair-distribution function) via a back-calculated Fourier transform (25). A major advantage of SAXS is that it can be applied to samples in solution, removing the requirement for crystals and thus artifacts frequently produced by crystal packing. As a result, SAXS can be used to study flexible and disordered proteins and protein fragments that are not amenable to x-ray crystallography. Interpretation of SAXS data usually involves computing theoretical SAXS profiles (26–28) for one or more atomic structures derived from x-ray crystallography, NMR spectroscopy, comparative modeling, or ab initio structure prediction. The computed profiles are compared to the experimental SAXS profiles to find a single or multiple structural models that are consistent with the data (29–34).

One of the main difficulties in applying SAXS analysis is obtaining a homogenous sample; even a low level of nonmonodispersity can interfere with the accuracy of SAXS data interpretation and may be difficult to detect. This problem is even more pronounced for amyloidogenic proteins that often display aggregation in the highly concentrated samples needed for SAXS data collection. One way proteins can be purified to a suitably high level of monodispersity is by size-exclusion chromatography (SEC) via fast protein liquid chromatography (FPLC), where the macromolecule is separated into fractions based on size and shape. Therefore, an SEC-FPLC system coupled directly with a SAXS beamline (FPLC-SAXS) has several advantages over traditional data-collection strategies: a high level of monodispersity can be obtained, monodispersity can be easily verified using the ultraviolet (UV) trace, and small differences in buffer constitution are averaged out when the sample flows through the column (35,36). For the work reported here, difficulties in obtaining pure monodisperse samples suitable for measurement using the autosampler setup motivated the development of an FPLC-SAXS system at Stanford Synchrotron Radiation Lightsource (SSRL) Beamline BL4-2 (37). FPLC-SAXS has now proved helpful for many unrelated projects and is now among the core protocols on the beamline (38–40).

Here, we present an FPLC-SAXS pipeline in which the SAXS profiles of fractionated PrP could be collected immediately after SEC separation. This pipeline, in combination with integrative atomic modeling of complexes (27,28,31), was used to characterize monomers of full-length and truncated recombinant PrP (recPrP(23–230) and recPrP(89–230), respectively) and their complexes with two Fab antibodies (P and R1). Models of the recPrP–Fab complexes provided insight into the mechanism of action of each Fab. Specifically, Fab-P binds to a region that is affected by structural reorganization (residues 95–105), and thus may prevent the PrP^{C}-to-PrP^{Sc} transition. Our model of the recPrP-Fab-R1 complex identified an additional interaction site (residues 165–175) that is known to influence the misfolding of PrP (41–43); R1 binding to this site may inhibit misfolding of PrP.

MATERIALS AND METHODS

Sample preparation and FPLC-SAXS measurements

Truncated recPrP(89–230) and recPrP(23–230), as well as Fab fragments of HuM-R1 and HuM-P, were overexpressed and purified as previously described (44,45) (Fig. S1 in the Supporting Material). Lyophilized recPrP(89–230) and recPrP(23–230) pellets were dissolved in distilled water and dialyzed two times against sodium acetate buffer (20 mM sodium acetate, pH 5.1, and 150 mM NaCl) at 4°C (46). PrP-Fab complexes were made by mixing recPrP with the antibodies and leaving them for 30 min at room temperature to equilibrate. For quality control, aliquots of the PrP samples or the PrP-Fab complexes were adjusted to 1× LDS sample buffer (nonreducing conditions) and incubated for 5 min at 95°C, after which sodium dodecyl sulfate polyacrylamide gel electrophoresis was performed using 4–12% Bis-Tris gradient gels (Invitrogen, Carlsbad, CA) followed by Coomassie stain (Invitrogen) (Fig. S1).

To mitigate aggregation, an FPLC-SAXS system was developed on SSRL Beamline BL4-2, utilizing an Ettan FPLC system (GE Healthcare, Little Chalfont, United Kingdom) connected to an autosampler via PEEK tubing (37). A Superdex PC3.2/200 SEC column was used to purify the protein, with a flow rate of 0.05 or 0.08 mL, depending on the protein's sensitivity to radiation damage. The column was equilibrated with one and one-half column volumes of running buffer (20 mM sodium acetate, pH 5.1, and 150 mM NaCl). A 100-μL sample loop was used, and for each data collection, a slight excess of sample (PrP alone, antibodies alone, and PrP-Fab complexes) was injected into the system. An x-ray scattering image was taken every second during most of the FPLC run. All SAXS data were collected with a nominal 1.7 m sample-to-detector distance, at 11 keV, with an exposure time of 1 s per image (Table 1).

FPLC-SAXS data processing and analysis

All data were collected using a Mar225 CCD detector. For each image, subtracted intensities were obtained using SasTool (47). For the autosampler data, the intensities from the buffer data were subtracted from the sample data to produce the final scattering profile (37). For the FPLC data, the first

TABLE 1 Summary of SAXS experiments

Data Collection	
Beamline	SSRL Beamline BL4-2
Defining slit size (mm)	0.3(H) × 0.3 (V)
Beam energy (keV)	11
Sample-detector distance (m)	1.7
Detector	Rayonix MX225-HE
Pixel binning	8 × 8
Pixel size (μm)	292
Exposure time (s)	1
Images	images taken for duration of run =~700 images
Type of sample cell	quartz capillary (diameter 1.5 mm)
Temperature (K)	283
Calibrant	AgBe
Final q range (Å^{-1})	0.01 to 0.5
Data Analysis	
Programs	SASTOOL (47), PRIMUS (48)
Buffer	20 mM Tris, 50 mM NaCl, pH 7.5
Injected protein concentrations (mg/mL)	see Table 2
Points used for Guinier analysis	see Table 2
Guinier qR_g limits	see Table 2
Guinier R_g (Å)	see Table 2
GNOM q range (Å^{-1})	see Table 2
D_{max} (Å)	see Table 2
R_g (real) (Å)	see Table 2
R_g (reciprocal) (Å)	see Table 2
Modeling	
Programs	IMP (rrt_sample, foxs, multi_foxs), Pymol
Data plotting	GNUPLOT

100 fraction images were used to create a combined buffer scattering profile, followed by subtracting the profile from each of the remaining images to produce the final scattering profile for each exposure. Data were initially analyzed using the ATSAS package (29). The scattering profiles for samples around peaks in UV absorbance (determined by UV-visible spectroscopy) (see Fig. 2) were selectively merged to produce the final SAXS profiles (Table 2). First, we selected a range of relevant SAXS profiles that were in the vicinity of the UV peak with low variance in both R_g and I_0 traces. Depending on the data, this range included 10–50 consecutive SAXS profiles. Second, we merged each non-overlapping window of 10 profiles in this range using Primus (48) and estimated the molecular weight based on the merged profile using SAXS MOW (49). Finally, we selected a merged profile with the best match to the molecular weight calculated from the sequence.

Computational modeling

Representation and scoring function

Atomic-resolution structural models were used for interpretation of the samples. The models were compared to the SAXS profiles using the FoXS method, which optimizes hydration layer density (c_2) and excluded volume (c_1) to improve the fit of a model to the experimental SAXS profile (27,28). The quality of the fit is assessed by the χ score (26):

$$\chi = \sqrt{\frac{1}{S}\sum_{i=1}^{S}\left(\frac{I_{exp}(q_i) - cI(q_i, c_1, c_2)}{\sigma(q_i)}\right)^2},$$

where $I_{exp}(q)$ is the experimental profile, $\sigma(q)$ is the experimental error of the measured profile, and S is the number of points in the profile. $I(q, c_1, c_2)$ is the computed profile, given by the Debye formula (27), with c, c_1, and c_2 optimized to minimize the score.

Here, we are also considering a possibility of a mixture of states contributing to the observed single SAXS profile. In such a case, the score of a multi-state model (a model that specifies two or more coexisting structural states and their population weights) is given by

$$\chi = \sqrt{\frac{1}{S}\sum_{i=1}^{S}\left(\frac{I_{exp}(q_i) - c\sum_{n} w_n I_n(q_i, c_1, c_2)}{\sigma(q_i)}\right)^2},$$

where $I_n(q, c_1, c_2)$ and w_n are the computed profile and the corresponding weight, respectively, for each of the N states in the model; this equation minimizes data overfitting by using a single set of c_1 and c_2 values for all N states.

TABLE 2 Summary of data analysis of the experimental SAXS profiles

Samples	Injected Concentration[a] (mg/mL)	FPLC Flow Rate (mL/min)	R_g (Real ± SD) (Å)	Guinier Points	q*R_g	D_{max} (Å)	Native Molecular Weight (kDa)	Molecular Weight Estimation[b] (kDa)	Porod Volume[c] (Å^3) (q-range (Å^{-1}))
recPrP(89–230)	3.6	0.05	21.84 ± 0.88	13–44	1.081	76.5	16.2	15.4	20,548 (0.010–0.255)
recPrP(23–230)	4.1	0.08	30.69 ± 1.20	1–18	0.495	104.4	22.9	26.0	39,832 (0.017–0.258)
Fab-P	5.3	0.05	26.86 ± 0.12	9–43	1.305	84.8	47.4	48.4	67,280 (0.010–0.150)
Fab-R1	4.1	0.05	26.25 ± 1.10	20–45	1.301	96.8	47.5	48.8	68,292 (0.010–0.142)
recPrP(89–230)-Fab-P	1.0 2.6	0.05	36.20 ± 0.57	3–15	0.850	121.1	63.6	68.6	84,955 (0.010–0.191)
recPrP(23–230)-Fab-P	1.0 3.7	0.08	38.90 ± 0.60	1–15	0.986	136.1	70.3	73.8	104,183 (0.013–0.217)
recPrP(89–230)-Fab-R1	1.0 3.7	0.05	34.40 ± 0.48	1–16	0.914	120.4	63.7	62.8	78,474 (0.013–0.197)
recPrP(23–230)-Fab-R1	1.0 2.9	0.08	33.20 ± 0.83	1–10	0.904	113.6	70.4	62.2	79,039 (0.019–0.205)

[a]We estimate that the eluted concentration at the beam capillary is ~67% of the corresponding injected concentration, according to UV spectroscopy (data not shown).
[b]Molecular weights were estimated using SAXS MOW (49) with a threshold of $Q_{max} = 0.25$ Å^{-1}.
[c]Porod volumes were calculated using DATPOROD in the ATSAS package (29). The q-ranges were evaluated using the porod function in PRIMUS (48).

Sampling of the disordered regions in recPrP

Initial models for the disordered regions were built using MODELER 9.13 (50). The disordered region of PrP (residues 23–125) was sampled using rapidly exploring random trees (RRTs) (51,52). The RRT algorithm samples the conformational space by leveraging an iteratively constructed nearest-neighbor linked tree. This iterative strategy expands the tree toward unexplored regions of the conformational space and significantly improves the sampling efficiency compared to random sampling. The φ and ψ angles of the disordered regions were sampled independently. We generated 10,000 models for each disordered region. To increase the confidence in the sampling protocol, we generated 50,000 models and validated that no other models with lower χ scores were produced in the ensemble.

Sampling of the Fab-P and Fab-R1 antibodies

The Fab models were generated using MODELER 9.13 (50) using different templates to account for 28 different Fab elbow angles (range 130–180°) (53). For each template, 10 models were generated and fitted to the experimental SAXS profile of the Fab using FoXS (27,28).

Sampling of the recPrP-Fab complexes

The computational modeling of the recPrP-Fab complexes was performed using an integrative docking protocol (54). To account for the flexibility of the C-terminal region, we used 20 conformations of recPrP from the solution NMR spectroscopy (Protein Data Bank (PDB) code 2L39) (16). Over 400,000 models were generated using the rigid-body docking program PatchDock with antibody-antigen protocol (55). The disordered N-terminal regions of recPrP(89–230) and recPrP(23–230) were not used in the docking stage, but subsequently were sampled using RRT and added for fitting to SAXS profiles using FoXS (27,28). The interface between the Fab-R1 and recPrP was scored with the SOAP-PP statistical potential (56). Each docking model was ranked by the sum of the Z-scores for the SAXS χ and SOAP-PP scores.

Multi-state model enumeration

Given N input conformations and their computed SAXS profiles, our goal was to find multi-state models of size n ($n << N$), such that the corresponding sum of weighted SAXS profiles fitted the experimental SAXS profile. Multi-state model enumeration was performed by MultiFoXS iteratively using the branch-and-bound method (57). In each branch step, we extended K ($K = 10{,}000$) best-scoring models of size n to KN models of size $n + 1$ by addition of each of the N input conformations. In the bound step, we selected K best-scoring models out of the total KN models for the next iteration. Therefore, generation of K multi-state models of size $n + 1$ from K multi-state models of size n required KN SAXS score calculations. This greedy approach avoided the exponential growth in scale of enumeration while still producing the good-scoring multi-state models.

RESULTS

Solution structures of full-length and N-terminally truncated recPrP

Previously, only residues 119–230 (mouse sequence) of full-length (residues 23–230) recPrP were structurally characterized by solution NMR spectroscopy and x-ray crystallography (12–14,16,17). Initial SAXS data collection was attempted on recPrP(89–230) and recPrP(23–230) at SSRL Beamline BL4-2 using an autosampler (37) (Fig. 1). The initial SAXS profiles indicated that both recPrP samples suffered from severe aggregation effects; all attempts to reduce aggregation via filtering, centrifugation, and ultracentrifugation failed (Fig. 1, *blue*). In comparison, FLPC-SAXS runs of recPrP(89–230) and recPrP(23–230) showed linearity in the Guinier region of the SAXS profiles (Fig. 1, *red*).

The radius of gyration (R_g) values calculated from the SAXS profiles were 21.8 ± 0.9 Å and 30.7 ± 1.2 Å for recPrP(89–230) and recPrP(23–230), respectively (Fig. 2, *A* and *B*, and Table 2). For comparison, the R_g

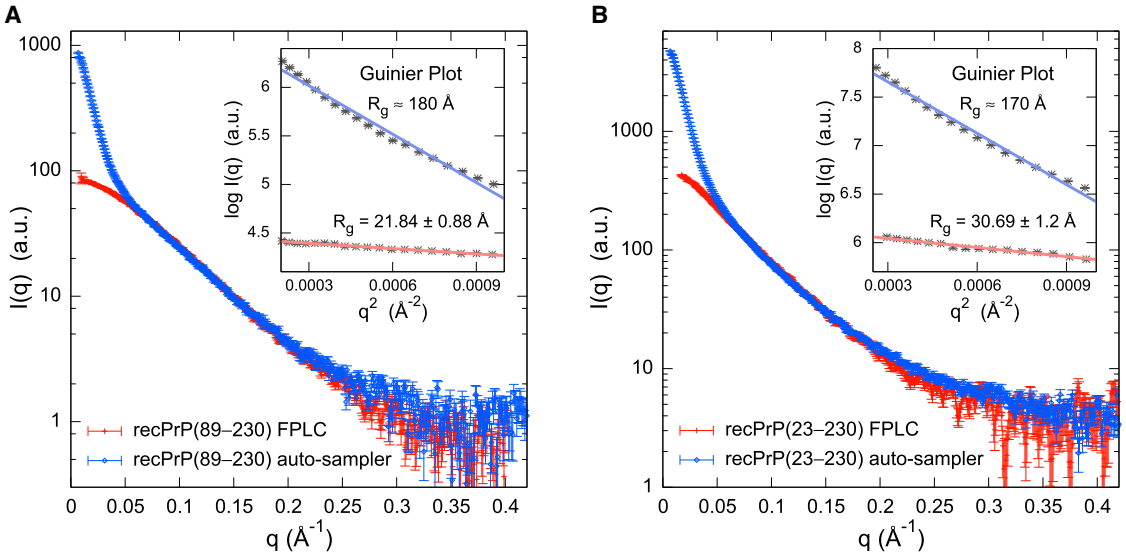

FIGURE 1 Comparison of the SAXS profiles obtained using FPLC and the SSRL BL4-2 autosampler. The SAXS profiles of (*A*) recPrP(89–230) and (*B*) recPrP(23–230) were collected using both FPLC (*red*) and the SSRL BL4-2 autosampler (*blue*). Data obtained from the SSRL BL4-2 autosampler showed that both protein samples suffered from severe aggregation effects, and any attempts to reduce this via filtering, centrifugation, and ultracentrifugation failed. In comparison, the SAXS profiles collected using FPLC showed linearity in the Guinier region (*insets*). To see this figure in color, go online.

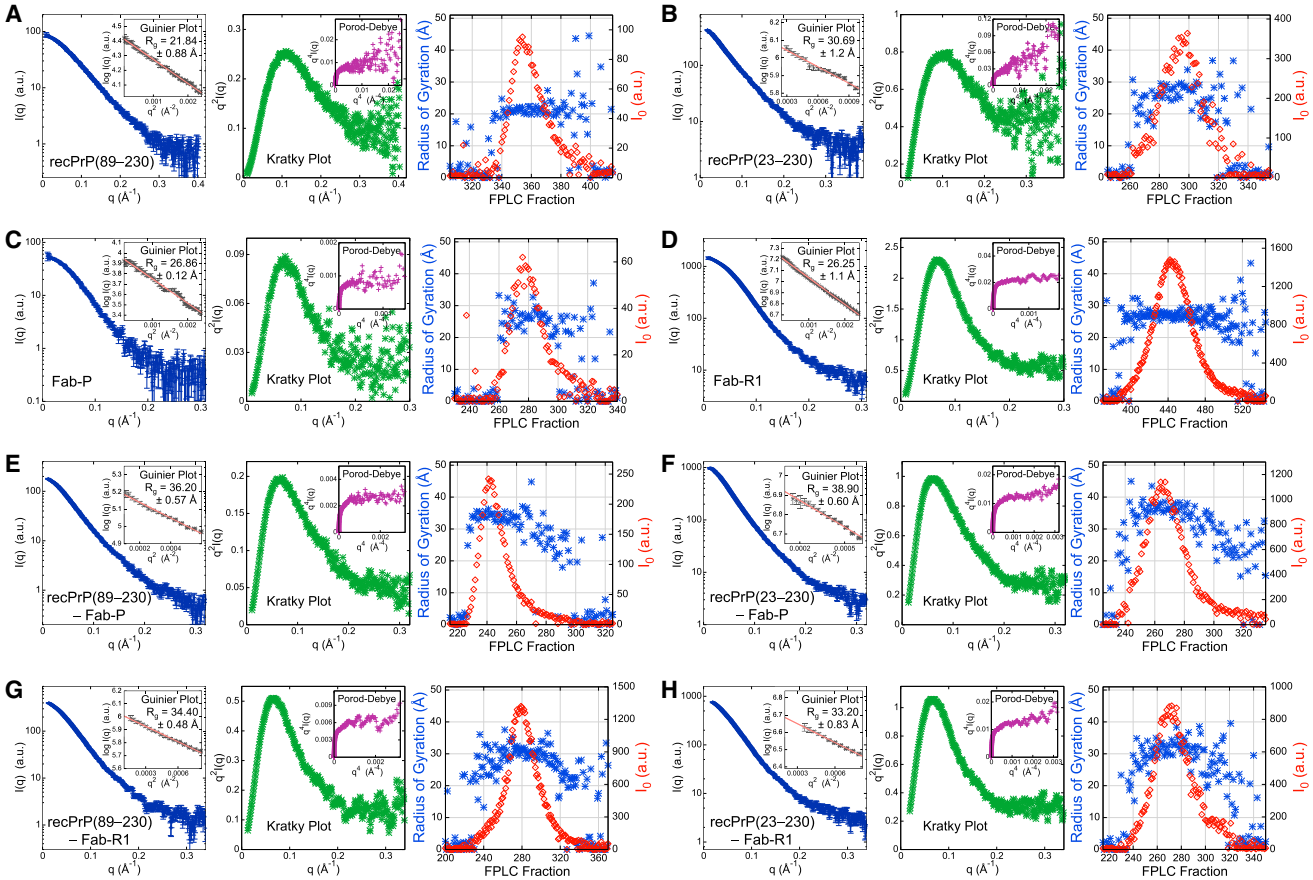

FIGURE 2 Summary of FPLC-SAXS data analysis. FPLC-SAXS data were obtained for (*A*) recPrP(89–230), (*B*) recPrP(23–230), (*C*) Fab-P, (*D*) Fab-R1, (*E*) the recPrP(89–230)-Fab-P complex, (*F*) the recPrP(23–230)-Fab-P complex, (*G*) the recPrP(89–230)-Fab-R1 complex, and (*H*) the recPrP(23–230)-Fab-R1 complex. For each sample, SAXS profiles (*left*), Kratky plots (*middle*), and FPLC traces (*right*) are shown. The SAXS profiles (*dark blue*) and the accompanying Guinier plot (*left inset*, *black dots*) are shown together. The radius of gyration (R_g) value was determined from a linear fit in the Guinier plot (*left inset*, *red line*). Porod-Debye plots (*middle inset*, *purple*) are shown for the corresponding SAXS profile, visually depicting the level of flexibility for the corresponding sample in solution. The FPLC traces of R_g (*blue*) and I_0 (*red*) are shown around the peak in UV absorbance for the corresponding sample (*right*). To see this figure in color, go online.

of recPrP(120–231) calculated from the solution NMR structure (PDB code 2L39) (16) was 15.0 Å; however, the structure lacks atomic coordinates for 31 and 97 disordered N-terminal residues compared to recPrP(89–230) and recPrP(23–230), respectively. The top 1000 of the 10,000 models generated by RRT had χ values from 1.33 to 3.05 for recPrP(89–230) (Fig. 3 *A*) and from 1.26 to 5.70 for recPrP(23–230) (Fig. 3 *B*). Thus, a single structural state explains the data within the data noise. However, it is unlikely that the system actually exists in a single conformation, given the failure of both NMR spectroscopy and x-ray crystallography to determine the structure of the N-terminal fragment (residues 23–125). Therefore, we enumerated possible *N*-state models, with *N* between 2 and 5, saving the 1000 top-scoring models for each *N*. The multi-state models fit the data within the noise with even better scores than any single-state model (a model that specifies a single structural state), as expected (because there are more degrees of freedom in these models to fit the data). The 1000 top-scoring two-state models had χ values from 1.19 to 1.22 for recPrP(89–230) (Fig. 3 *A*) and from 1.01 to 1.20 for recPrP(23–230) (Fig. 3 *B*). There was no significant improvement in the χ scores for models of three or more states.

In an effort to characterize the range of conformations consistent with the SAXS data, we analyzed distributions of the R_g for the entire ensemble of 10,000 conformations as well as the 1000 best-scoring *N*-state models ($N = 1 \ldots 5$). For recPrP(89–230), the R_g peak was 22 Å for the entire ensemble of conformations and 21 Å for the single-state models; two R_g peaks (18 Å and 24 Å) were conserved among the best-scoring *N*-state models for *N* from 2 to 5 (Fig. 3 *E*). Similar distributions were observed for recPrP(23–230) (Fig. 3 *F*). For both recPrP constructs, the first R_g peak (~60–70% of the population) corresponded to compact closed conformations, whereas the second peak (~30–40%) corresponded to extended open conformations

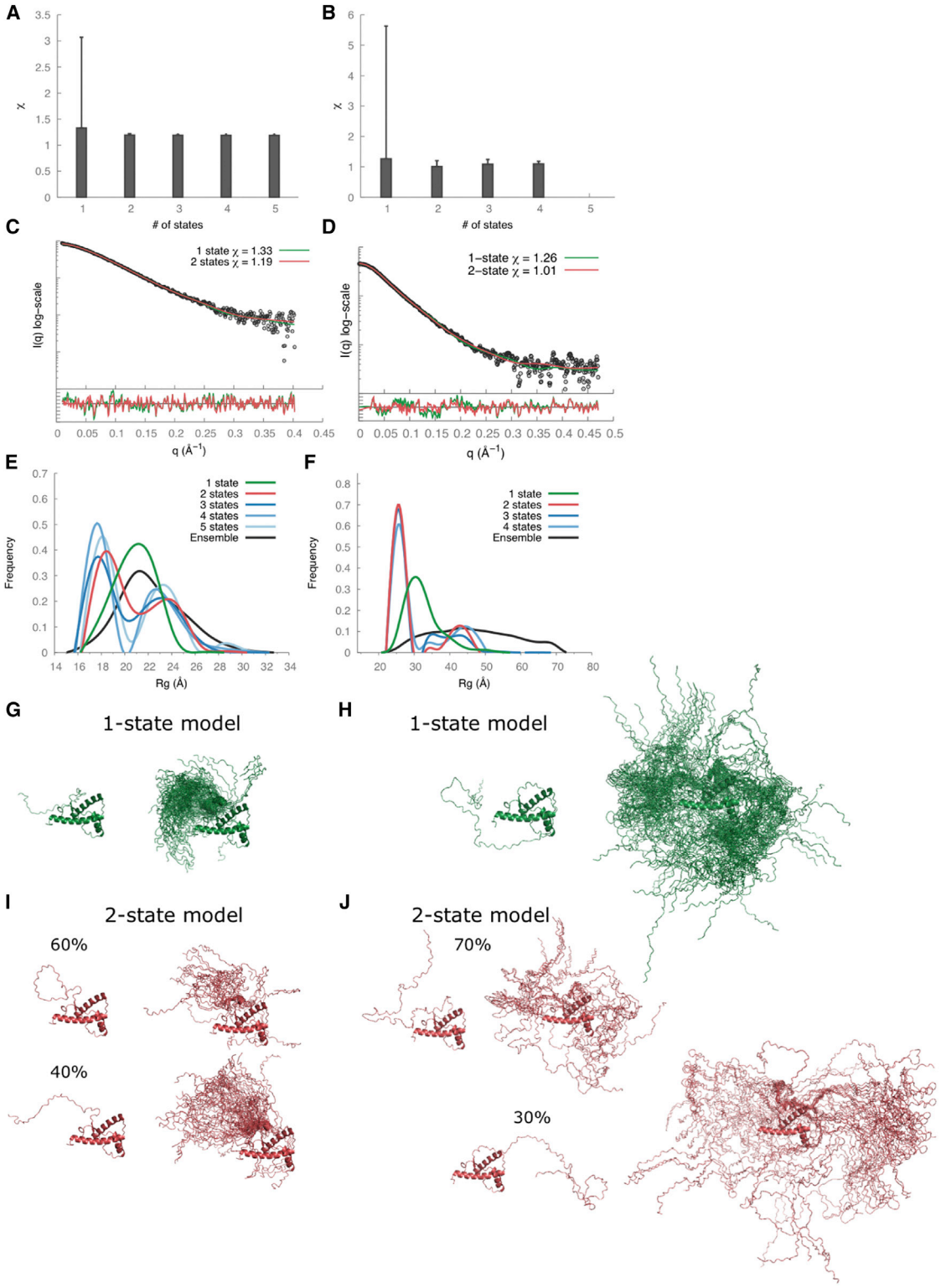

FIGURE 3 SAXS data analysis and modeling for recPrP(89–230) (*left column*) and recPrP(23–230) (*right column*). (*A* and *B*) The lowest χ scores for each of the *N*-state models ($N = 1$–5) are shown with an error bar indicating the range of χ values for the top 1000 models. (*C* and *D*) Comparison of the experimental SAXS profiles (*black*) with computed SAXS profiles for the top-scoring single-state (*green*) and two-state (*red*) models. The lower plots show the residuals defined as $(I_{exp}(q) - I_{calc}(q))/\sigma_{exp}(q)$, corresponding to the difference between the experimental and the computed intensities weighted by the experimental uncertainty. (*E* and *F*) R_g distributions for the entire ensemble of 10,000 conformations and the top 1000 *N*-state models are shown. (*G–J*) Conformations of the top-scoring single-state (*G* and *H*) and two-state models (*I* and *J*) are shown on the left, and the top 100 models aligned on the structured C-terminal domain of PrP^C on the right. To see this figure in color, go online.

(Fig. 3, *I* and *J*). In other words, each one of the two states contained many different conformations with similar R_g values.

Solution structures of humanized antibody fragments Fab-P and Fab-R1

There are multiple Fab structures deposited in the PDB, including the structure of HuM-P (PDB code 2HH0) (58). A change in the elbow angle results in a different orientation between the constant and variable Fab domains, and subsequently in a significant difference in the distance distribution function. Therefore, accurate modeling of the elbow angle was necessary to obtain a good fit to the SAXS profile. The x-ray structure of HuM-P Fab (PDB code 2HH0) (58) has an elbow angle of 128° and a χ score of 1.79. Our model of Fab-P with the lowest χ score of 1.30 had an elbow angle of 177°, indicating that its solution state might be different from the crystallographic state (Fig. 4 *A*). Similarly, a Fab-R1 model with the lowest χ score of 1.65 also had an elbow angle of 177° (Fig. 4 *B*). The R_g values calculated from the SAXS profiles were 26.9 ± 0.1 Å and 26.3 ± 1.1 Å for Fab-P and Fab-R1, respectively (Fig. 2, *C* and *D*, and Table 2).

Solution structures of recPrP(89–230)-Fab-P and recPrP(23–230)-Fab-P complexes

The SAXS profiles of recPrP(89–230)-Fab-P and recPrP(23–230)-Fab-P were subtly different, with R_g values of 36.2 ± 0.6 Å and 38.9 ± 0.6 Å, respectively (Fig. 2, *E* and *F*, and Table 2). An initial model of the complex was obtained using a PDB structure of Fab-P associated with the epitope peptide from PrP (PDB code 2HH0) (58), adding the missing linker residues (either 89–94 or 23–94, and 105–124) to the prion structure (using MODELER 9.13 (50)). The elbow angle of the Fab was set to 177° to be consistent with the solution Fab state.

The top 1000 of the 10,000 models generated using RRT had χ values from 1.28 to 2.11 for the recPrP(89–230)-Fab-P complex (Fig. 5 *A*) and from 2.13 to 6.00 for the recPrP(23–230)-Fab-P complex (Fig. 5 *B*). As with recPrP alone, we explored a single-state model as well as *N*-state models (N = 2–5) for both complexes. A single-state model fit the data within the noise only for the recPrP(89–230)-Fab-P complex, but not for the recPrP(23–230)-Fab-P complex (Fig. 5, *C* and *D*). For the two-state models, both recPrP(89–230)-Fab-P

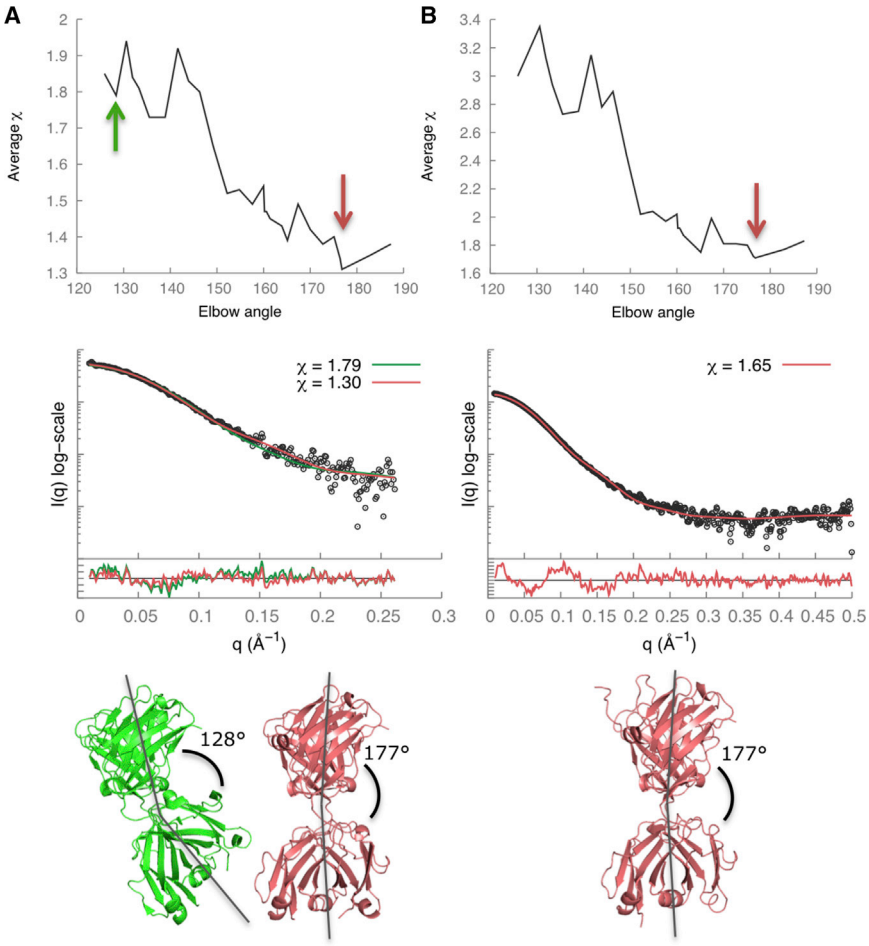

FIGURE 4 SAXS data analysis and modeling for (*A*) Fab-P and (*B*) Fab-R1. The Fab elbow angle versus χ score (*upper*), the SAXS profile fits and the residual plots (*middle*), and the best-scoring structural models (*lower*, *red*) are shown. The lowest χ scores were 1.30 for Fab-P and 1.65 for Fab-R1. In (*A*, *lower*), the x-ray crystal structure of Fab-P (*green*; PDB code 2HH0; χ = 1.79; elbow angle 128°) (58) was compared to the best-scoring model of Fab-P (*red*; χ = 1.30; elbow angle 177°). To see this figure in color, go online.

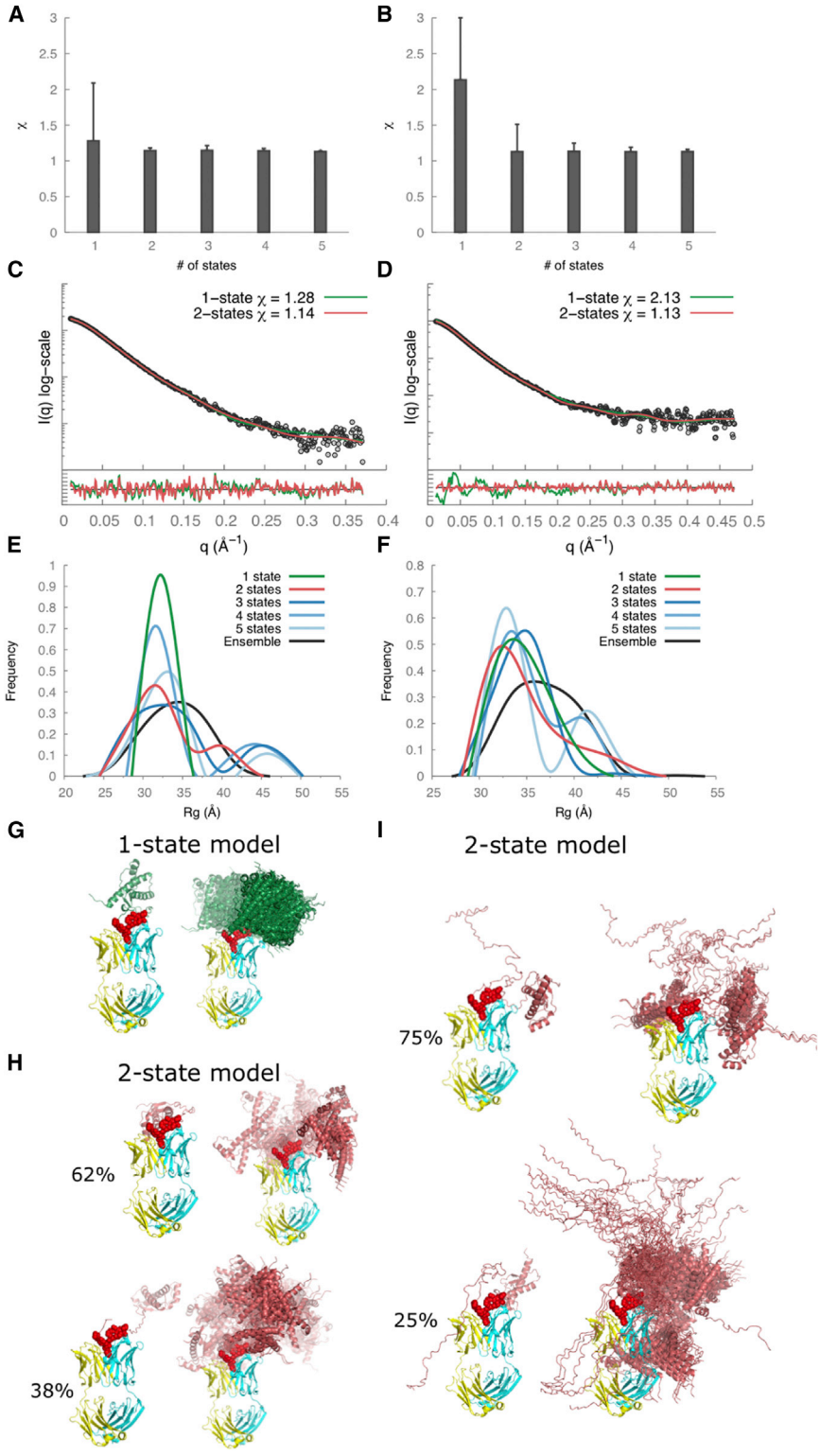

FIGURE 5 SAXS data analysis and modeling for the recPrP(89–230)-Fab-P (*left column*) and recPrP(23–230)-Fab-P complexes (*right column*). (*A* and *B*) The lowest χ scores for each of the *N*-state models ($N = 1$–5) are shown with error bars indicating the range of χ values for the top 1000 models. (*C* and *D*) Comparison of the experimental SAXS profiles (*black*) with the computed SAXS profiles for the top-scoring single-state (*green*) and two-state (*red*) models. The lower plots show the residuals defined as $(I_{exp}(q) - I_{calc}(q))/\sigma_{exp}(q)$, corresponding to the difference between the experimental and computed intensities weighted by the experimental uncertainty. (*E* and *F*) R_g distributions for the entire ensemble of 10,000 conformations and the top 1000 *N*-state models are shown. (*G–I*) Conformations of the top-scoring single-state (*G*) and two-state models (*H* and *I*) are shown on the left and the top 100 models aligned on the Fab structure on the right. The heavy chain of Fab is shown in cyan, the light chain in yellow, and the epitope residues in red space-fill. To see this figure in color, go online.

and recPrP(23–230)-Fab-P complexes fit the data within the noise. The 1000 top-scoring two-state models had χ values from 1.14 to 1.18 for recPrP(89–230)-Fab-P (Fig. 5 *A*) and from 1.13 to 1.51 for recPrP(23–230)-Fab-P (Fig. 5 *B*). Again, there was no significant improvement in the χ score for models of three or more states (Fig. 5, *A* and *B*).

In an effort to characterize the range of conformations consistent with the SAXS data, we analyzed distributions of the R_g for the entire ensemble of 10,000 conformations

as well as the 1000 best-scoring N-state models ($N = 1 \ldots 5$). For the recPrP(89–230)-Fab-P complex, the R_g peak was 35 Å for the entire ensemble of conformations and 32 Å for the single-state models (Fig. 5 *E*). For the best-scoring N-state models ($N = 2 \ldots 5$), two R_g peaks at 31 Å and 43 Å were conserved (Fig. 5 *E*). Similar distributions were observed for the recPrP(23–230)-Fab-P complex (Fig. 5 *F*). For both recPrP-Fab-P complexes, the first R_g peak (~60–75% of the population) corresponded to compact closed conformations, whereas the second peak (25–40%) corresponded to extended open conformations (Fig. 5, *H* and *I*). Similar to recPrP alone, each one of the two states for these recPrP-Fab complexes contains many different conformations with similar R_g.

Solution structures of recPrP(89–230)-Fab-R1 and recPrP(23–230)-Fab-R1 complexes

In contrast to Fab-P, which binds in the disordered linker region in the N-terminus, Fab-R1 binds at the C-terminal structured region (residues 223–230). Thus, the resulting complexes were more compact, with R_g values of ~34.0 Å for both recPrP(89–230)-Fab-R1 and recPrP(23–230)-Fab-R1 complexes (Fig. 2, *G* and *H*, and Table 2). The samples used for SAXS experiments remained intact, with no degradation products found under denaturing conditions by sodium dodecyl sulfate polyacrylamide gel electrophoresis (Fig. S1). However, for the recPrP(23–230)-Fab-R1 complex, the R_g value was determined using only 10 data points ($qR_g < 0.9$ (Table 2)), potentially explaining why we did not observe a significant difference between the R_g values for the two complexes. The epitope residues 223–230 were used as the site for computational docking, resulting in a single top-scoring cluster with an average C_α root mean-square deviation of 2.1 Å between each model in the cluster (Fig. 6 *E*); we use this variability as a measure of model precision. The model in each cluster with the best fit to the SAXS profile had a χ score of 1.33 for the recPrP(89–230)-Fab-R1 Fab complex (Fig. 6 *A*) and 1.46 for the recPrP(23–230)-Fab-R1 complex (Fig. 6 *B*). Of the recPrP interface residues, 75% corresponded to the known Fab-R1 epitope site (residues 221–230), whereas the remaining interface residues came from the $\alpha 2$-$\beta 2$ loop (residues 165–175).

DISCUSSION

The FPLC-SAXS enables measurement of a non-monodispersed sample

PrP^C has been difficult to study due to the difficulty of obtaining large amounts of purified protein from mammalian sources (10,59). Furthermore, natural PrP is anchored to the neuronal membranes via a glycosylphosphatidylinositol anchor (10,60), usually requiring preparations with lipids or detergents that render them inaccessible to SAXS-based studies (10,59). Structural comparison between natural and recombinant PrP did not reveal major structural differences; therefore, recombinant PrP can be used to study the PrP^C isoform in vitro (59,61).

Here, we demonstrate that an FPLC-SAXS system enabled collection of SAXS data on challenging protein samples (Figs. 1 and 2), and this system facilitate further work on recombinant multimerization-prone proteins, or indeed any system that can be purified to homogeneity with FPLC. In addition, FPLC-SAXS has the advantage of minimizing differences between the protein buffer and buffer measurements due to the continuous FPLC flow, helping to minimize potential radiation damage. These advantages allowed us to collect and interpret SAXS data for recPrP(89–230)-antibody and recPrP(23–230)-antibody complexes.

Although FPLC-SAXS allows collection of high-quality SAXS data sets that do not suffer from aggregation and compositional heterogeneity, the sample can still be conformationally heterogeneous, making data interpretation challenging. Usually, the best explanation of the data is obtained by minimizing the number of conformations that resulted in the data (Occam's razor) (33). For most of our samples, we found that a single conformation explains the SAXS data within its noise (Figs. 3 and 5). However, we know that PrP^C is almost certain to be conformationally heterogeneous in solution (thus, Occam's razor as expressed above does not apply here). To explicitly model this heterogeneity, we analyzed the data with multi-state models. Here, a multi-state model consists of multiple conformations and their weights; thus, the data are interpreted through the weighted combination of all states in a model, not any single state. We overcame the challenge of the resulting overfitting by computing ensembles of multi-state models that fit the data, using MultiFoXS (see Materials and Methods), and highlighting only the conserved features of these ensembles. Other similar approaches include EOM (62,63), MaxOcc (64–67), ASTEROIDS (68–70), SES (71), and EROS (72). A parsimonious explanation of the SAXS profiles for each of the recPrP and recPrP-Fab-P samples is provided by the open and closed states, corresponding to the two R_g peaks that were conserved for N-state models (for $N = 2 \ldots 5$; Figs. 3 and 5). Each of the two states consists of multiple different conformations with similar R_g values.

Possible inhibitory mechanisms of prion conversion by Fab-P and Fab-R1

Both Fab-P and Fab-R1 inhibit conversion from PrP^C to PrP^{Sc} but bind to different sites on PrP (19). Fab-P binds a region of PrP that is structurally accessible in PrP^C but not in PrP^{Sc} (73), whereas the epitope of Fab-R1 is accessible in both isoforms (74). Structural models of the recPrP-Fab-P and recPrP-Fab-R1 complexes were built

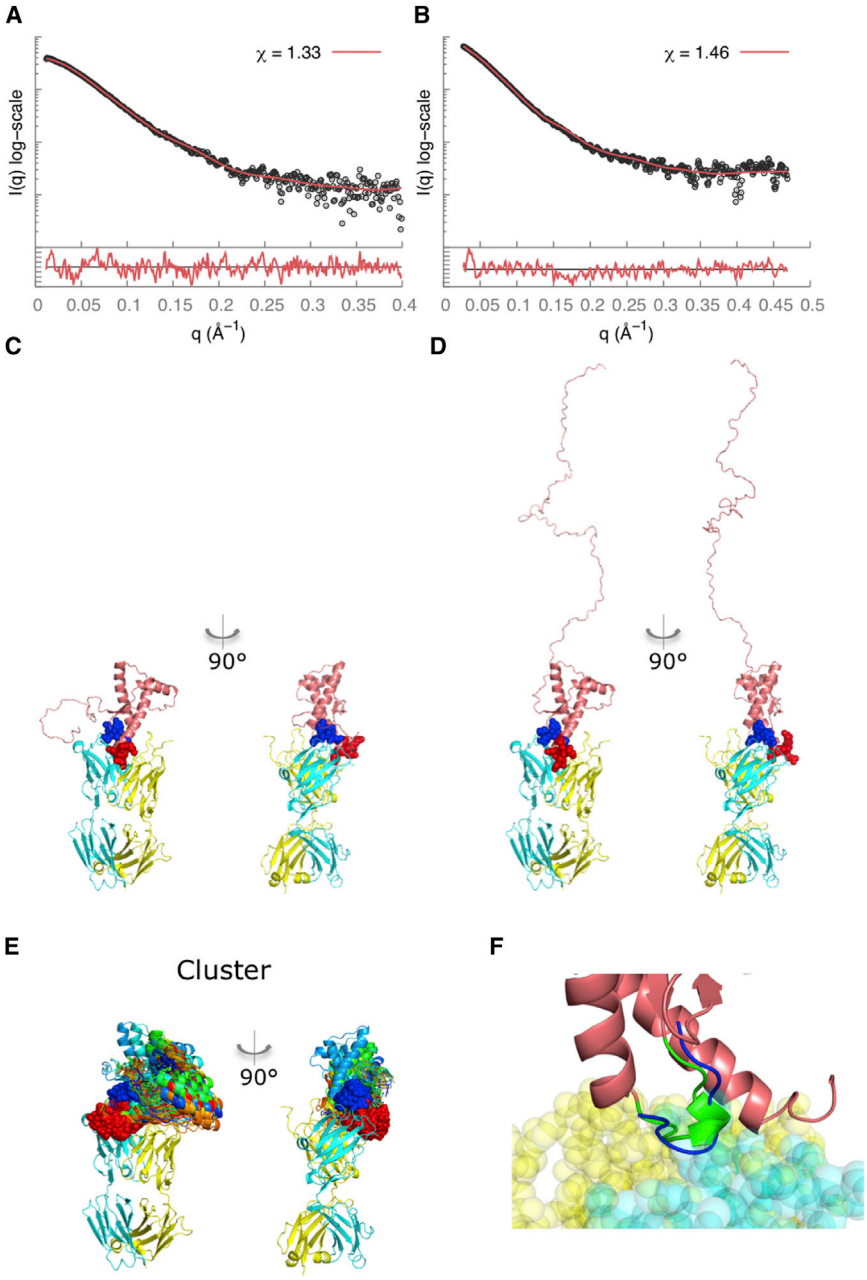

FIGURE 6 SAXS data analysis and modeling for the recPrP(89–230)-Fab-R1 (*left column*) and recPrP(23–230)-Fab-R1 (*right column*) complexes. The SAXS profile fits (*A* and *B*) and the corresponding best-scoring structural models (*C* and *D*) are shown for each of the samples. The lower plots in (*A*) and (*B*) show the residuals defined as $(I_{exp}(q) - I_{calc}(q))/\sigma_{exp}(q)$, corresponding to the difference between the experimental and computed intensities weighted by the experimental uncertainty. (*E*) The cluster of the top-scoring models is shown. The heavy chain of the Fab is shown in cyan, the light chain in yellow, and the epitope residues in red spacefill; the rigid loop is shown in blue. (*F*) Our structural model reveals interactions of the $\alpha2$-$\beta2$ loop of PrP^C (residues 165–175) with Fab-R1 (spacefill model) (41–43). This loop region in murine PrP^C exists in two structural states, a highly populated state that forms a 3_{10}-helical turn (*green*) and a minor state that forms a type-I β-turn (*blue*) (41,43). To see this figure in color, go online.

computationally by integrating information from SAXS profiles, known epitopes (45), structures from NMR spectroscopy and x-ray crystallography (16,58), as well as statistical potentials (56).

Based on our structural models, we speculate how each antibody prevents the conversion, as follows. Fab-P binds to the N-terminal region (residues 95–105) that is known to undergo structural conversion from PrP^C to PrP^{Sc}. The Fab-P might prevent the PrP^C-PrP^{Sc} interaction by acting as a structural clamp on the epitope, thus preventing its conversion from the disordered conformation in PrP^C to the ordered β-sheet conformation in PrP^{Sc}. Given the size of Fab-P relative to PrP, the Fab-P-PrP interaction could also interfere with the refolding of PrP^C into PrP^{Sc} outside of the epitope.

In contrast to Fab-P, Fab-R1 binds to residues 225–230, whose conformation probably does not change during the conversion, allowing for binding of both PrP^C and PrP^{Sc}. The interaction of Fab-R1 with both isoforms of PrP^C and PrP^{Sc} might sterically inhibit a crucial interaction between PrP^C and PrP^{Sc}. In addition to the known Fab-R1 epitope of PrP^C, our structural model revealed putative contacts between Fab-R1 and PrP residues 165–175, the $\alpha2$-$\beta2$ loop of PrP^C (41–43). This loop region in murine PrP exists in two structural states, a major state that forms a 3_{10}-helical turn and a minor state that forms a type-I β-turn (41,43)

(Fig. 6 *F*). Interestingly, the sequence of this loop region has also been shown to be strongly associated with the rate of prion infection (41–43). Our structural model rationalizes this observation, suggesting that Fab-R1 prevents or slows down the conversion from PrP^{C} to PrP^{Sc} by influencing the structure and/or dynamics of the $\alpha 2$-$\beta 2$ loop.

Alternatively, the binding of either Fab-P or Fab-R1 may be sufficient to divert PrP^{C} from conversion into PrP^{Sc} by accelerating its degradation (75,76). It may be possible to determine whether this explanation applies to either or both of the PrP^{C}-Fab complexes described here. Radiolabeling of nascent PrP^{C} and measuring its turnover may help extend our understanding of the mechanism by which anti-PrP antibodies inhibit PrP^{Sc} formation (77,78).

CONCLUSIONS

The FPLC-SAXS pipeline presented here minimizes data artifacts caused by a non-monodispersed sample, enabling high-quality data collection on challenging macromolecular systems that are prone to aggregation. We applied this approach toward structural characterization of recPrP, both on its own and in complex with two different antibodies. Based on the resulting structural models, we propose two different mechanisms for antibody-mediated inhibition of the PrP^{C}-to-PrP^{Sc} conversion: 1) direct inhibition by Fab-P binding to a PrP^{C} region (residues 95–105) known to undergo rearrangement during PrP^{C}-to-PrP^{Sc} conversion (74); and 2) indirect inhibition by Fab-R1 that is predicted here to bind to the $\alpha 2$-$\beta 2$ loop structure (residues 165–175), which is known to impact the conversion rate (41–43). As noted above, antibody-mediated inhibition of PrP^{Sc} formation may also occur through accelerating the degradation of PrP^{C}.

Although anti-Aβ antibody therapies for Alzheimer's disease have been widely tested, none have been successful. Because $<0.1\%$ of systemically administered antibodies cross the blood-brain barrier, the use of anti-Aβ antibodies to treat or prevent Alzheimer's disease is probably a poor strategy. The same problems apply for antibody therapeutics for PrP prion diseases: Anti-PrP antibodies have not extended the lives of mice inoculated intracerebrally (79), but they have prolonged the lives of mice inoculated intraperitoneally (80). Whether the structural insights reported here prove useful in facilitating the discovery of therapeutically effective small molecules remains to be determined.

SUPPORTING MATERIAL

One figure is available at http://www.biophysj.org/biophysj/supplemental/S0006-3495(15)00708-0.

AUTHOR CONTRIBUTIONS

L.C., S.J.K., D.S.-D., J.S., T.M.W., H.T., S.B.P., and A.S. designed the research; J.S., G.P.-M., and S.B.P. prepared samples for data collection; L.C., S.J.K., T.M.W., and H.T. collected SAXS data; L.C., S.J.K., D.S.-D., and J.S. analyzed the data; D.S.-D., S.J.K., and A.S. performed computational modeling; and L.C., S.J.K., D.S.-D., J.S., S.B.P., and A.S. wrote the article.

ACKNOWLEDGMENTS

The contents of this publication are solely the responsibility of the authors and do not necessarily represent the official views of the National Center for Research Resources or the National Institutes of Health.

Funding for this work was provided by National Institutes of Health grants R01 GM083960 and P41 GM109824. Portions of this research were carried out at the Stanford Synchrotron Radiation Lightsource, a Directorate of the SLAC National Accelerator Laboratory and an Office of Science User Facility operated for the U.S. Department of Energy Office of Science by Stanford University. The SSRL Structural Molecular Biology Program is supported by the U.S. Department of Energy Office of Biological and Environmental Research, and by the National Institutes of Health, National Center for Research Resources, Biomedical Technology Program (P41 RR001209).

REFERENCES

1. Prusiner, S. B. 2012. Cell biology. A unifying role for prions in neurodegenerative diseases. *Science.* 336:1511–1513.
2. Colby, D. W., and S. B. Prusiner. 2011. Prions. *Cold Spring Harb. Perspect. Biol.* 3:a006833.
3. Walker, L. C., M. I. Diamond, …, B. T. Hyman. 2013. Mechanisms of protein seeding in neurodegenerative diseases. *JAMA Neurol.* 70:304–310.
4. Walker, L. C., and M. Jucker. 2013. Seeds of dementia. *Sci. Am.* 308:52–57.
5. Prusiner, S. B. 2013. Biology and genetics of prions causing neurodegeneration. *Annu. Rev. Genet.* 47:601–623.
6. Weissmann, C., and A. Aguzzi. 2005. Approaches to therapy of prion diseases. *Annu. Rev. Med.* 56:321–344.
7. Prusiner, S. B. 1982. Novel proteinaceous infectious particles cause scrapie. *Science.* 216:136–144.
8. Pan, K.-M., M. Baldwin, …, S. B. Prusiner. 1993. Conversion of α-helices into β-sheets features in the formation of the scrapie prion proteins. *Proc. Natl. Acad. Sci. USA.* 90:10962–10966.
9. Pergami, P., H. Jaffe, and J. Safar. 1996. Semipreparative chromatographic method to purify the normal cellular isoform of the prion protein in nondenatured form. *Anal. Biochem.* 236:63–73.
10. Pan, K. M., N. Stahl, and S. B. Prusiner. 1992. Purification and properties of the cellular prion protein from Syrian hamster brain. *Protein Sci.* 1:1343–1352.
11. Nicolas, O., R. Gavín, and J. A. del Río. 2009. New insights into cellular prion protein (PrPc) functions: the "ying and yang" of a relevant protein. *Brain Res. Brain Res. Rev.* 61:170–184.
12. Riek, R., S. Hornemann, …, K. Wüthrich. 1996. NMR structure of the mouse prion protein domain PrP(121–231). *Nature.* 382:180–182.
13. James, T. L., H. Liu, …, F. E. Cohen. 1997. Solution structure of a 142-residue recombinant prion protein corresponding to the infectious fragment of the scrapie isoform. *Proc. Natl. Acad. Sci. USA.* 94:10086–10091.
14. Donne, D. G., J. H. Viles, …, H. J. Dyson. 1997. Structure of the recombinant full-length hamster prion protein PrP(29–231): the N terminus is highly flexible. *Proc. Natl. Acad. Sci. USA.* 94:13452–13457.
15. Knaus, K. J., M. Morillas, …, V. C. Yee. 2001. Crystal structure of the human prion protein reveals a mechanism for oligomerization. *Nat. Struct. Biol.* 8:770–774.

16. Damberger, F. F., B. Christen, …, K. Wüthrich. 2011. Cellular prion protein conformation and function. *Proc. Natl. Acad. Sci. USA.* 108:17308–17313.

17. Baral, P. K., M. Swayampakula, …, M. N. James. 2014. Structural basis of prion inhibition by phenothiazine compounds. *Structure.* 22:291–303.

18. Wille, H., W. Bian, …, G. Stubbs. 2009. Natural and synthetic prion structure from x-ray fiber diffraction. *Proc. Natl. Acad. Sci. USA.* 106:16990–16995.

19. Peretz, D., R. A. Williamson, …, S. B. Prusiner. 2002. Antibodies inhibit prion formation and abolish prion infectivity. *In* Transmissible Spongiform Encephalopathies: New Perspectives for Prion Therapeutics. S. Lehmann, editor. Editions de Condé, Paris, France, pp. 107–118.

20. Klöhn, P. C., M. Farmer, …, J. Collinge. 2012. PrP antibodies do not trigger mouse hippocampal neuron apoptosis. *Science.* 335:52.

21. Solforosi, L., J. R. Criado, …, R. A. Williamson. 2004. Cross-linking cellular prion protein triggers neuronal apoptosis in vivo. *Science.* 303:1514–1516.

22. Putnam, C. D., M. Hammel, …, J. A. Tainer. 2007. X-ray solution scattering (SAXS) combined with crystallography and computation: defining accurate macromolecular structures, conformations and assemblies in solution. *Q. Rev. Biophys.* 40:191–285.

23. Mertens, H. D., and D. I. Svergun. 2010. Structural characterization of proteins and complexes using small-angle x-ray solution scattering. *J. Struct. Biol.* 172:128–141.

24. Jacques, D. A., and J. Trewhella. 2010. Small-angle scattering for structural biology—expanding the frontier while avoiding the pitfalls. *Protein science.* 19:642–657.

25. Svergun, D. 1992. Determination of the regularization parameter in indirect-transform methods using perceptual criteria. *J. Appl. Crystallogr.* 25:495–503.

26. Svergun, D., C. Barberato, and M. H. J. Koch. 1995. CRYSOL—a program to evaluate x-ray solution scattering of biological macromolecules from atomic coordinates. *J. Appl. Crystallogr.* 28:768–773.

27. Schneidman-Duhovny, D., M. Hammel, and A. Sali. 2010. FoXS: a web server for rapid computation and fitting of SAXS profiles. *Nucleic Acids Res.* 38:W540–W544.

28. Schneidman-Duhovny, D., M. Hammel, …, A. Sali. 2013. Accurate SAXS profile computation and its assessment by contrast variation experiments. *Biophys. J.* 105:962–974.

29. Petoukhov, M. V., P. V. Konarev, …, D. I. Svergun. 2007. ATSAS 2.1 - towards automated and web-supported small-angle scattering data analysis. *J. Appl. Crystallogr.* 40:S223–S228.

30. Pons, C., M. D'Abramo, …, J. Fernández-Recio. 2010. Structural characterization of protein-protein complexes by integrating computational docking with small-angle scattering data. *J. Mol. Biol.* 403:217–230.

31. Schneidman-Duhovny, D., M. Hammel, and A. Sali. 2011. Macromolecular docking restrained by a small angle x-ray scattering profile. *J. Struct. Biol.* 173:461–471.

32. Bernadó, P., Y. Pérez, …, M. Pons. 2008. Structural characterization of the active and inactive states of Src kinase in solution by small-angle x-ray scattering. *J. Mol. Biol.* 376:492–505.

33. Pelikan, M., G. L. Hura, and M. Hammel. 2009. Structure and flexibility within proteins as identified through small angle x-ray scattering. *Gen. Physiol. Biophys.* 28:174–189.

34. Hammel, M. 2012. Validation of macromolecular flexibility in solution by small-angle x-ray scattering (SAXS). *Eur. Biophys. J.* 41:789–799.

35. Mathew, E., A. Mirza, and N. Menhart. 2004. Liquid-chromatography-coupled SAXS for accurate sizing of aggregating proteins. *J. Synchrotron Radiat.* 11:314–318.

36. Pérez, J., and Y. Nishino. 2012. Advances in x-ray scattering: from solution SAXS to achievements with coherent beams. *Curr. Opin. Struct. Biol.* 22:670–678.

37. Martel, A., P. Liu, …, H. Tsuruta. 2012. An integrated high-throughput data acquisition system for biological solution x-ray scattering studies. *J. Synchrotron Radiat.* 19:431–434.

38. Trastoy, B., J. V. Lomino, …, E. J. Sundberg. 2014. Crystal structure of Streptococcus pyogenes EndoS, an immunomodulatory endoglycosidase specific for human IgG antibodies. *Proc. Natl. Acad. Sci. USA.* 111:6714–6719.

39. Ho, M. C., C. Wilczek, …, D. Shechter. 2013. Structure of the arginine methyltransferase PRMT5-MEP50 reveals a mechanism for substrate specificity. *PLoS One.* 8:e57008.

40. West, A. L., S. E. Evans, …, S. L. Michel. 2012. Ni(II) coordination to mixed sites modulates DNA binding of HpNikR via a long-range effect. *Proc. Natl. Acad. Sci. USA.* 109:5633–5638.

41. Christen, B., F. F. Damberger, …, K. Wüthrich. 2013. Structural plasticity of the cellular prion protein and implications in health and disease. *Proc. Natl. Acad. Sci. USA.* 110:8549–8554.

42. Kyle, L. M., T. R. John, …, R. V. Lewis. 2013. Introducing a rigid loop structure from deer into mouse prion protein increases its propensity for misfolding in vitro. *PLoS One.* 8:e66715.

43. Kurt, T. D., C. Bett, …, C. J. Sigurdson. 2014. Prion transmission prevented by modifying the $\beta2$-$\alpha2$ loop structure of host PrPC. *J. Neurosci.* 34:1022–1027.

44. Mehlhorn, I., D. Groth, …, S. B. Prusiner. 1996. High-level expression and characterization of a purified 142-residue polypeptide of the prion protein. *Biochemistry.* 35:5528–5537.

45. Williamson, R. A., D. Peretz, …, D. R. Burton. 1998. Mapping the prion protein using recombinant antibodies. *J. Virol.* 72:9413–9418.

46. Poncet-Montange, G., S. J. St Martin, …, S. Ghaemmaghami. 2011. A survey of antiprion compounds reveals the prevalence of non-PrP molecular targets. *J. Biol. Chem.* 286:27718–27728.

47. SasTool. 2013. http://ssrl.slac.stanford.edu/~saxs/analysis/sastool.htm.

48. Konarev, P. V., V. V. Volkov, …, D. I. Svergun. 2003. PRIMUS: a Windows PC-based system for small-angle scattering data analysis. *J. Appl. Crystallogr.* 36:1277–1282.

49. Fischer, H., M. D. Neto, …, A. F. Craievich. 2010. Determination of the molecular weight of proteins in solution from a single small-angle x-ray scattering measurement on a relative scale. *J. Appl. Crystallogr.* 43:101–109.

50. Sali, A., and T. L. Blundell. 1993. Comparative protein modelling by satisfaction of spatial restraints. *J. Mol. Biol.* 234:779–815.

51. Amato, N. M., and G. Song. 2002. Using motion planning to study protein folding pathways. *J. Comput. Biol.* 9:149–168.

52. Raveh, B., A. Enosh, …, D. Halperin. 2009. Rapid sampling of molecular motions with prior information constraints. *PLOS Comput. Biol.* 5:e1000295.

53. Stanfield, R. L., A. Zemla, …, B. Rupp. 2006. Antibody elbow angles are influenced by their light chain class. *J. Mol. Biol.* 357:1566–1574.

54. Schneidman-Duhovny, D., A. Rossi, …, A. Sali. 2012. A method for integrative structure determination of protein-protein complexes. *Bioinformatics.* 28:3282–3289.

55. Schneidman-Duhovny, D., Y. Inbar, …, H. J. Wolfson. 2005. PatchDock and SymmDock: servers for rigid and symmetric docking. *Nucleic Acids Res.* 33:W363–W367.

56. Dong, G. Q., H. Fan, …, A. Sali. 2013. Optimized atomic statistical potentials: assessment of protein interfaces and loops. *Bioinformatics.* 29:3158–3166.

57. Lawler, E. L., and D. E. Wood. 1966. Branch-and-bound methods: a survey. *Oper. Res.* 14:699–719.

58. Luginbühl, B., Z. Kanyo, …, A. Plückthun. 2006. Directed evolution of an anti-prion protein scFv fragment to an affinity of 1 pM and its structural interpretation. *J. Mol. Biol.* 363:75–97.

59. Elfrink, K., J. Ollesch, …, K. Gerwert. 2008. Structural changes of membrane-anchored native PrP^C. *Proc. Natl. Acad. Sci. USA.* 105:10815–10819.

60. Baldwin, M. A., N. Stahl, …, S. B. Prusiner. 1992. Glycosylinositol phospholipid anchors of prion proteins. *In* Prion Diseases of Humans and Animals. S. B. Prusiner, J. Collinge, J. Powell, and B. Anderton, editors. Ellis Horwood, London, pp. 380–397.

61. Hornemann, S., C. Schorn, and K. Wüthrich. 2004. NMR structure of the bovine prion protein isolated from healthy calf brains. *EMBO Rep.* 5:1159–1164.

62. Bernadó, P., E. Mylonas, …, D. I. Svergun. 2007. Structural characterization of flexible proteins using small-angle x-ray scattering. *J. Am. Chem. Soc.* 129:5656–5664.

63. Bernadó, P., and D. I. Svergun. 2012. Structural analysis of intrinsically disordered proteins by small-angle x-ray scattering. *Mol. Biosyst.* 8:151–167.

64. Bertini, I., A. Giachetti, …, D. I. Svergun. 2010. Conformational space of flexible biological macromolecules from average data. *J. Am. Chem. Soc.* 132:13553–13558.

65. Bertini, I., L. Ferella, …, D. I. Svergun. 2012. MaxOcc: a web portal for maximum occurrence analysis. *J. Biomol. NMR.* 53:271–280.

66. Cerofolini, L., G. B. Fields, …, J. M. Teixeira. 2013. Examination of matrix metalloproteinase-1 in solution: a preference for the pre-collagenolysis state. *J. Biol. Chem.* 288:30659–30671.

67. Andrałojć, W., C. Luchinat, …, E. Ravera. 2014. Exploring regions of conformational space occupied by two-domain proteins. *J. Phys. Chem. B.* 118:10576–10587.

68. Nodet, G., L. Salmon, …, M. Blackledge. 2009. Quantitative description of backbone conformational sampling of unfolded proteins at amino acid resolution from NMR residual dipolar couplings. *J. Am. Chem. Soc.* 131:17908–17918.

69. Salmon, L., G. Nodet, …, M. Blackledge. 2010. NMR characterization of long-range order in intrinsically disordered proteins. *J. Am. Chem. Soc.* 132:8407–8418.

70. Fisher, C. K., and C. M. Stultz. 2011. Constructing ensembles for intrinsically disordered proteins. *Curr. Opin. Struct. Biol.* 21:426–431.

71. Berlin, K., C. A. Castañeda, …, D. Fushman. 2013. Recovering a representative conformational ensemble from underdetermined macromolecular structural data. *J. Am. Chem. Soc.* 135:16595–16609.

72. Różycki, B., Y. C. Kim, and G. Hummer. 2011. SAXS ensemble refinement of ESCRT-III CHMP3 conformational transitions. *Structure.* 19:109–116.

73. Peretz, D., R. A. Williamson, …, D. R. Burton. 1997. A conformational transition at the N terminus of the prion protein features in formation of the scrapie isoform. *J. Mol. Biol.* 273:614–622.

74. Govaerts, C., H. Wille, …, F. E. Cohen. 2004. Evidence for assembly of prions with left-handed β-helices into trimers. *Proc. Natl. Acad. Sci. USA.* 101:8342–8347.

75. Enari, M., E. Flechsig, and C. Weissmann. 2001. Scrapie prion protein accumulation by scrapie-infected neuroblastoma cells abrogated by exposure to a prion protein antibody. *Proc. Natl. Acad. Sci. USA.* 98:9295–9299.

76. Peretz, D., R. A. Williamson, …, S. B. Prusiner. 2001. Antibodies inhibit prion propagation and clear cell cultures of prion infectivity. *Nature.* 412:739–743.

77. Caughey, B., R. E. Race, …, B. Chesebro. 1989. Prion protein biosynthesis in scrapie-infected and uninfected neuroblastoma cells. *J. Virol.* 63:175–181.

78. Borchelt, D. R., M. Scott, …, S. B. Prusiner. 1990. Scrapie and cellular prion proteins differ in their kinetics of synthesis and topology in cultured cells. *J. Cell Biol.* 110:743–752.

79. Ohsawa, N., C.-H. Song, …, M. Horiuchi. 2013. Therapeutic effect of peripheral administration of an anti-prion protein antibody on mice infected with prions. *Microbiol. Immunol.* 57:288–297.

80. White, A. R., P. Enever, …, S. Hawke. 2003. Monoclonal antibodies inhibit prion replication and delay the development of prion disease. *Nature.* 422:80–83.

Supporting Materials
Biophysical Journal, Volume 109, August 2015
http://dx.doi.org/10.1016/j.bpj.2015.06.065

Prion protein–antibody complexes characterized by chromatography-coupled small-angle X-ray scattering

Lester Carter[1]*, Seung Joong Kim[2]*, Dina Schneidman-Duhovny[2]*, Jan Stöhr[3,4]*, Guillaume Poncet-Montange[3‡], Thomas M. Weiss[1], Hiro Tsuruta[1]**, Stanley B. Prusiner[3,4†], and Andrej Sali[2†]

[1]Stanford Synchrotron Radiation Lightsource, SLAC National Accelerator Laboratory, 2575 Sand Hill Road, Menlo Park, CA 94025, USA

[2]Department of Bioengineering and Therapeutic Sciences, Department of Pharmaceutical Chemistry, and California Institute for Quantitative Biosciences (QB3), University of California San Francisco, 1700 4th Street, Byers Hall Room 503B, San Francisco, CA 94158, USA

[3]Institute for Neurodegenerative Diseases and [4]Department of Neurology, University of California San Francisco, 675 Nelson Rising Ln, Room 316, San Francisco, CA 94143-0518, USA

[‡]Current address: Department of Genomic Medicine, University of Texas, MD Anderson Cancer Center, 1515 Holcombe Blvd. Unit 1000, Houston, TX 77030, USA

**These authors contributed equally to this work.*

***Deceased on August 25, 2011

[†]Corresponding Authors: Andrej Sali: sali@salilab.org; Stanley Prusiner: stanley@ind.ucsf.edu

Running Title: PrP-antibody complex structures by FPLC-SAXS

Keywords: prion; Fab antibody; fast protein liquid chromatography; small-angle X-ray scattering; rapidly exploring random trees; structural biology.

Supporting Materials
Biophysical Journal, Volume 109, August 2015
http://dx.doi.org/10.1016/j.bpj.2015.06.065

GLOSSARY

PrP: prion protein

PrP^{C}: cellular isoform of the prion protein

PrP^{Sc}: infectious isoform of the prion protein

recPrP: recombinant PrP

full-length recPrP: recombinant PrP of mouse sequence 23–230

truncated recPrP: recombinant PrP of mouse sequence 89–230

FPLC: fast protein liquid chromatography

SAXS: small-angle X-ray scattering

SEC: size-exclusion chromatography

RRT: rapidly exploring random trees

state: structural conformation with its associated population weight

single-state model: a model that specifies a single structural state

multi-state model: a model that specifies two or more co-existing structural states and their population weights

Supporting Materials
Biophysical Journal, Volume 109, August 2015
http://dx.doi.org/10.1016/j.bpj.2015.06.065

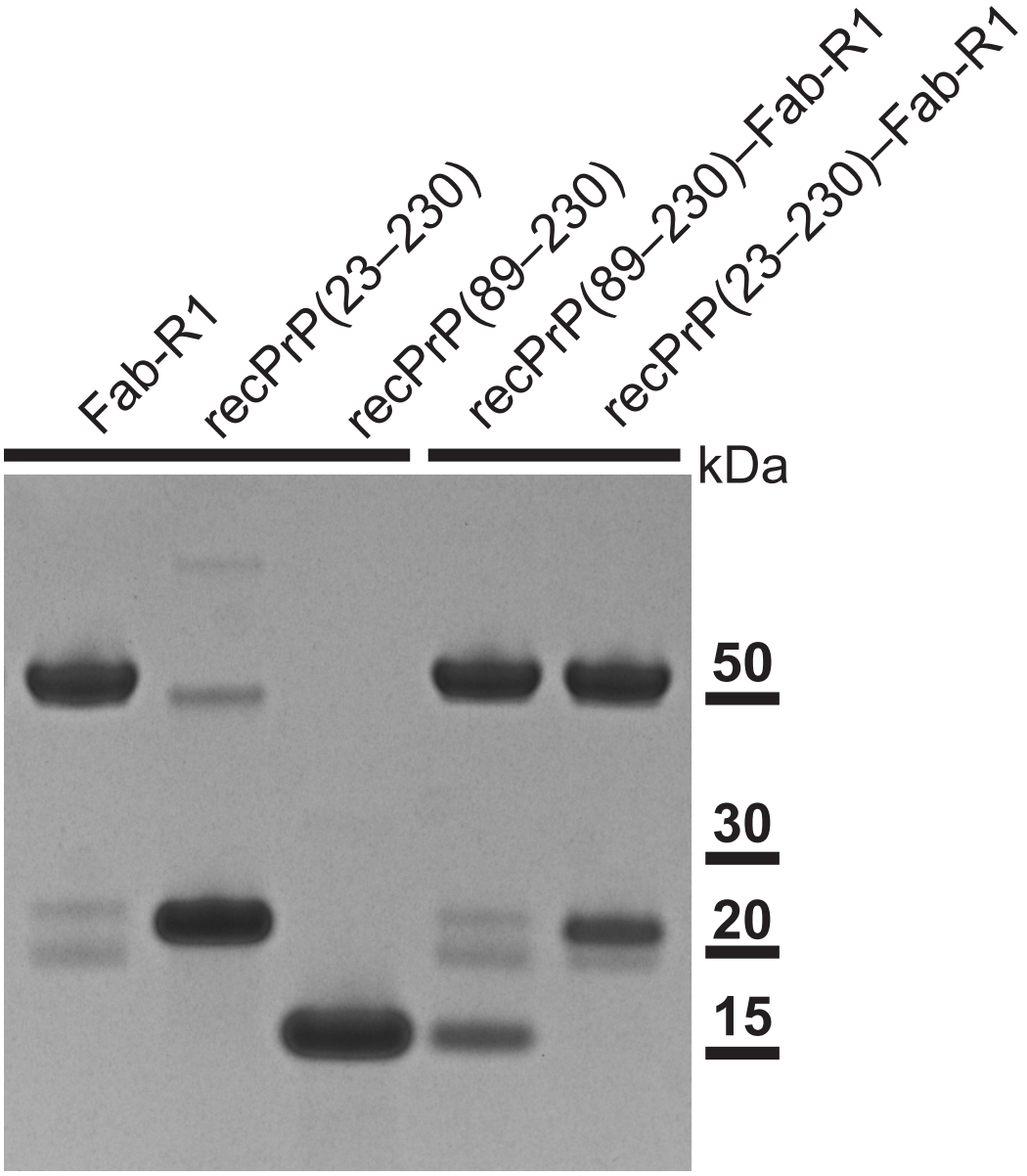

Supplemental Figure S1. **SDS-PAGE shows Fab-R1, recPrP, and recPrP–Fab-R1 complexes.** Samples were subjected to denaturing and nonreducing conditions and run on a SDS-PAGE showing highly purified samples with no contaminants detectable.